Supplementary Information for

'The Growing Charge-Density-Wave Order in CuTe Lightens and Speeds up Electrons'

I-Ta Wang[1,2,3,4†], Ta-Lei Chou[1,2†], Chih-En Hsu[5], Zhujialei Lei[6], Li-Min Wang[6], Ping-Hui Lin[7], Chih-Wei Luo[8], Chun-Wei Chen[3,4,9], Chia-Nung Kuo[10], Chin Shan Lue[10,11,12], Cheng-Hsuan Chen[1], Hung-Chung Hsueh[5*] & Ming-Wen Chu[1,2*]

[1]Center for Condensed Matter Sciences, National Taiwan University, Taipei 10617, Taiwan

[2]Center of Atomic Initiative for New Materials, National Taiwan University, Taipei 10617, Taiwan

[3]International Graduate Program of Molecular Science and Technology, National Taiwan University (NTU-MST), Taipei 10617, Taiwan

[4]Molecular Science and Technology Program, Taiwan International Graduate Program (TIGP), Academia Sinica, Taipei 11529, Taiwan

[5]Department of Physics, Tamkang University, New Taipei 251301, Taiwan

[6]Department of Physics, National Taiwan University, Taipei 10617, Taiwan

[7]National Synchrotron Radiation Research Center, Hsinchu 30076, Taiwan

[8]Department of Electrophysics, National Yang Ming Chiao Tung University, Hsinchu 30010, Taiwan

[9]Department of Materials Science and Engineering, National Taiwan University, Taipei 10617, Taiwan

[10]Department of Physics, National Cheng Kung University, Tainan 70101, Taiwan

[11]Taiwan Consortium of Emergent Crystalline Materials, National Science and Technology Council, Taipei 10601, Taiwan

[12]Program on Key Materials, Academy of Innovative Semiconductor and Sustainable Manufacturing, National Cheng Kung University, Tainan 70101, Taiwan

[†]The two authors contribute equally to this work.

[*]To whom correspondence should be addressed:
hchsueh@gms.tku.edu.tw & chumingwen@ntu.edu.tw

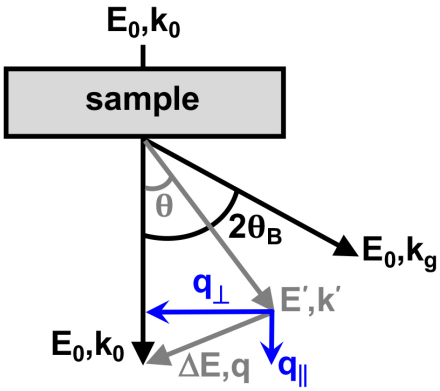

Supplementary Figure 1 | The inelastic electron scattering upon q-EELS. The inelastic scattering (gray) for plasmon excitations is subject to the respective energy and momentum transfers of ΔE and q, with respect to the incident electron beam (energy, E_0; wave vector, k_0)[1]. The elastic Bragg scattering (wave vector, k_g) is also indicated. The q vector consists of the $q_\parallel$ and $q_\perp$, with $\mathbf{q}_\parallel = \mathbf{k}_0\theta_{\Delta E}$ ($\theta_{\Delta E} = \frac{\Delta E}{2E_0}$). The $\theta_{\Delta E}$ is far smaller than the Bragg scattering angle ($2\theta_B$) and casts the $q_\parallel$ vector being very small. The q for q-EELS is, therefore, largely dominated by the $q_\perp$ with $\mathbf{q}_\perp = \mathbf{k_0}\theta$ and $\mathbf{q} = \sqrt{\mathbf{q}_\perp^2 + \mathbf{q}_\parallel^2}$. The $q_\perp$ is typically larger than the associated experimental momentum resolution Δq ($\Delta q \gg q_\parallel$) and leads to the condition of $\mathbf{q} = \sqrt{\mathbf{q}_\perp^2 + \mathbf{q}_\parallel^2} \approx \mathbf{q}_\perp$, which forms the scattering basis of the q-EELS experimental setup. Details, supplementary information A.

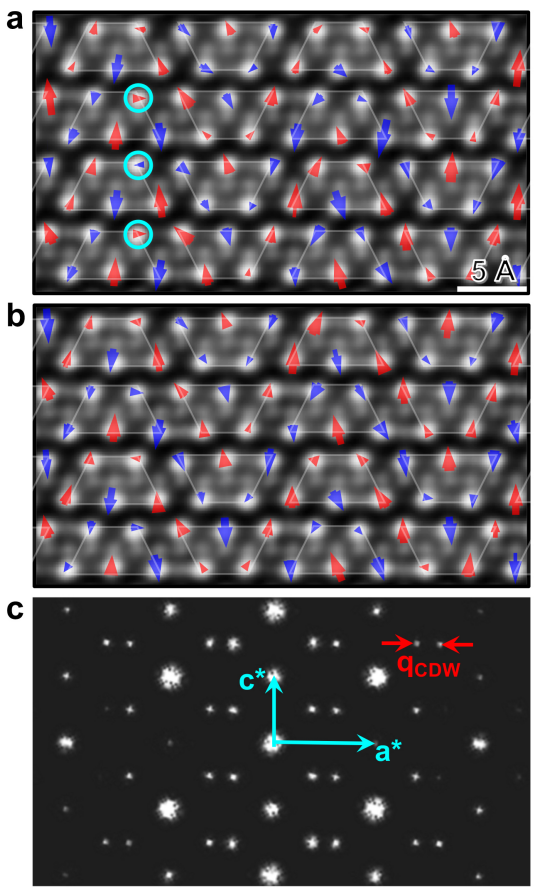

Supplementary Figure 2 | The STEM imaging and power spectrum of the CDW-state CuTe at 300 K. a, A CDW-state image from a sample region neighboring to Fig. 1b (main text). Arrows, the Te-atomic displacements (see Fig. 1b, main text). Trapezoids, guides for the eyes. Upon the image acquisition, unavoidable mechanical noises due to finite sample drifts and vibrations are registered and lead to the sign inversion of atomic-displacement arrows from blue (red) to red (blue) as indicated by the cyan circles. The mechanical noises also result in the imperfection in the arrow-size repetition with the anticipated CDW superperiodicity of 5a × 2c. **b**, The CDW-state image corresponding to Fig. 1b (main text), immune from the arrow-sign inversion in **a** while still preserving the imperfect arrow-size repetition. **c**, The power spectrum of the parent image comprising **a** and **b**, revealing the robust registration of the 5a × 2c superperiodicity in the image as the observed superlattice reflections in Fig. 2b (main text) despite the persistence of unavoidable mechanical noises. Our picometer-level evaluations of the atomic displacements make these effects of unavoidable and, meanwhile, very small mechanical noises easily observable.

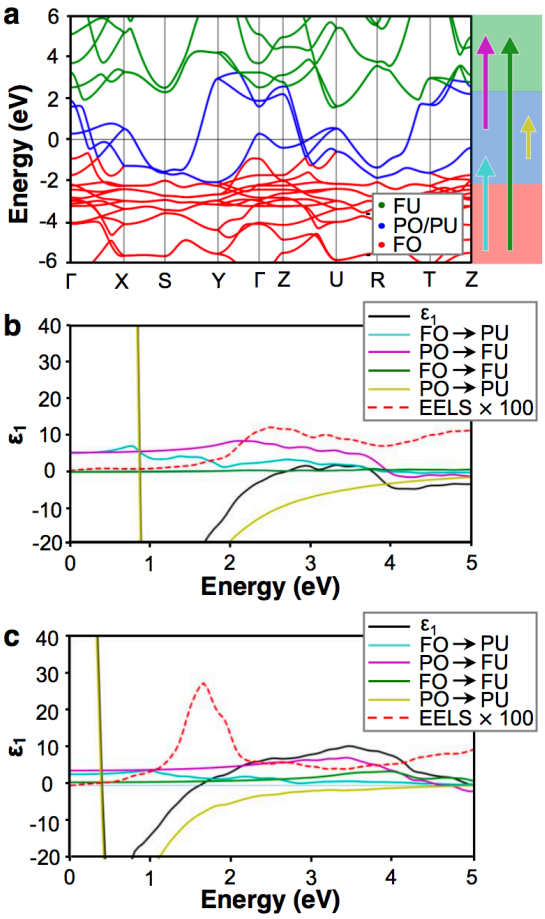

Supplementary Figure 3 | Correlations of intraband transitions with the light-electron and heavy-hole plasmons. a, Decomposition of the electronic structure into three categories of polarizability matrices: fully occupied (FO; red), partially occupied/unoccupied (PO/PU; blue), and fully unoccupied (FU; green) bands. Arrows, four types of pertinent single-particle transitions. Cyan arrow, the interband transition from FO to PU states. Purple arrow, the interband transition from PO to FU states. Dark green arrow, the interband transition from FO to FU states. Light olive arrow, the intraband transition from PO to PU states. **b** and **c**, Breakdowns of the real part of the complex dielectric functions (ε_1, black) along respective ΓX and ΓY into individual contributions from the interband and intraband transitions (color codes, same as **a**). Results in **b** and **c**, calculated at q = 0.1 Å^{-1}. Dashed red curves, the theoretical EELS loss functions multiplied by 100 for clarity of the presentation. The EELS-spectral onset at $\varepsilon_1 = 0$ (black) indicates the collective plasmon excitation. The light-electron plasmon in **b** and heavy-hole plasmon in **c** are primarily correlated with the respective intraband transitions (light olive) of Te-p_x and -p_x bands considering the corresponding ε_1 (light olive) represents the only zero-cross component in support of a plasmon excitation. The other three interband-transition ε_1 components (cyan, purple, and dark green) play the role of screening the intraband-transition one (light olive), leading to the condition of $\varepsilon_1 = 0$ of the total electronic contributions (black) taking place at a much lower energy than that of the sole intraband transition (light olive).

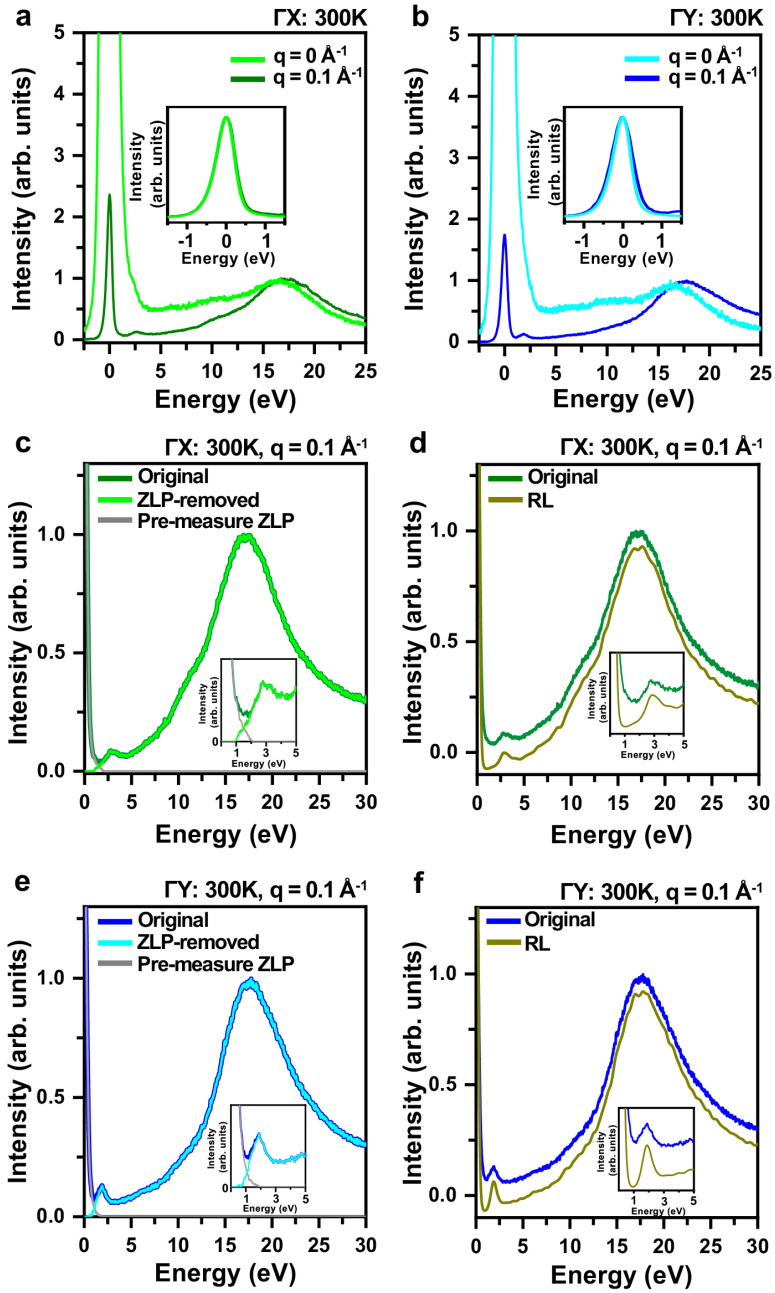

Supplementary Figure 4 | The ΓX light-electron and ΓY heavy-hole plasmons at q = 0 and 0.1 Å^{-1} at 300 K. The intense tails at q = 0 Å^{-1} in **a** and **b** due to the dynamical nature of electron scattering and finite momentum resolution of our apparatus mask the plasmon excitations that are essentially an order of magnitude weaker than the bulk plasmons (supplementary Figs. 5c, 5d, and 9). Spectral intensities, normalized to those of the bulk-plasmon excitations for the convenience of comparisons. By breaking the dynamical-scattering condition that is most prominent at q = 0 Å^{-1} through the off-q setup (such as q = 0.1 Å^{-1} hereby; meanwhile, having preserved the same momentum resolution), the intense tails can be significantly diminished and the light-electron and heavy-hole plasmons become resolvable. The persistent zero-loss peak (ZLP) at q = 0.1 Å^{-1} and also larger q's is assisted by the electron-phonon scattering, which prevails throughout the entire

Brillouin zone[2]. Insets, the otherwise normalizations of the spectral intensities to the ZLPs, showing that the ZLP widths only marginally increase at q = 0.1 $Å^{-1}$ upon the longer acquisition time required for the weaker plasmon excitations at this q. **c** and **e**, The ZLP removal by the method of fitting pre-measured ZLP for the respective light-electron and heavy-hole plasmons at q = 0.1 $Å^{-1}$ in **a** and **b**. Both the minimal overlap of the ZLP tail with the light-electron and heavy-hole plasmon peaks (insets) and the robustness of the plasmon-peak positions to the ZLP removal can be observed. **d** and **f**, The comparison of Richardson-Lucy (RL) deconvoluted[3,4] and original spectra of the respective light-electron and heavy-hole plasmons at q = 0.1 $Å^{-1}$, with the spectral-intensity normalizations to the bulk-plasmon excitations. The deconvoluted spectra are shifted downwards for the clarity of presentations. The RL deconvolutions have been conducted using the DeConvEELS package by HREM Research (https://www.hremresearch.com/msa/)[4]. Arrows, the artificial spectral ripples introduced by the RL deconvolutions. The RL deconvolutions improve the energy resolution to ~0.45 eV and sharpen the plasmons, of which the respective peak positions largely remain intact (insets). Nonetheless, the wavy spectral artifacts (arrows) discount the overall quality of the RL deconvolutions and the RL method is, therefore, not adopted.

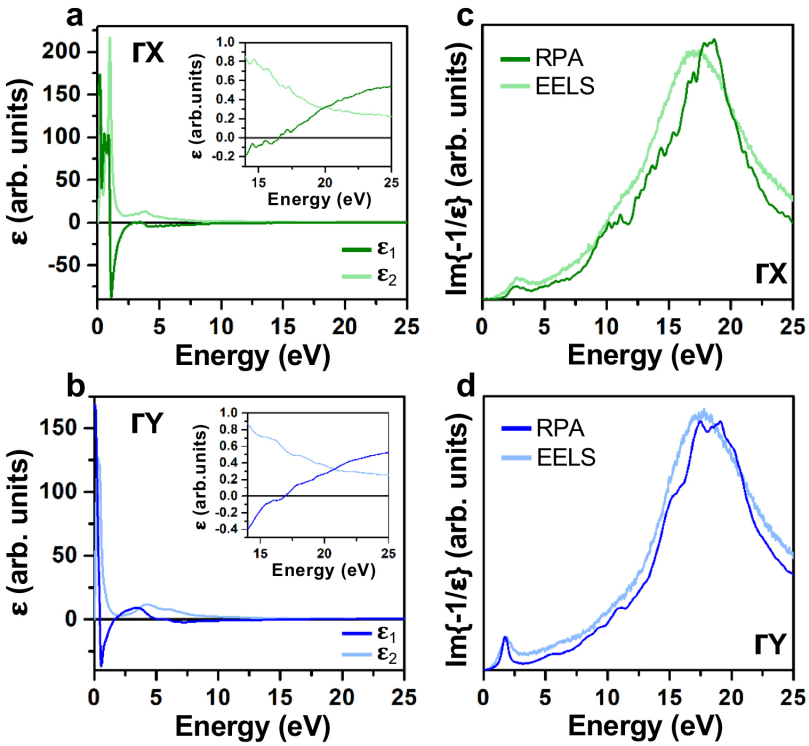

Supplementary Figure 5 | Theoretical complex dielectric functions and EELS loss functions of the CDW-state CuTe. a and **b**, The complex dielectric functions ($\varepsilon = \varepsilon_1 + i\varepsilon_2$) calculated within the framework of RPA at q = 0.1 Å^{-1} along ΓX and ΓY, respectively. Insets, blowups of the respective bulk-plasmon regimes, showing the absence of notable single-particle transitions above the collective-excitation onsets at $\varepsilon_1 = 0$. **c** and **d**, The RPA-derived loss functions and experimental EELS spectra at 0.1 Å^{-1} along ΓX and ΓY, respectively.

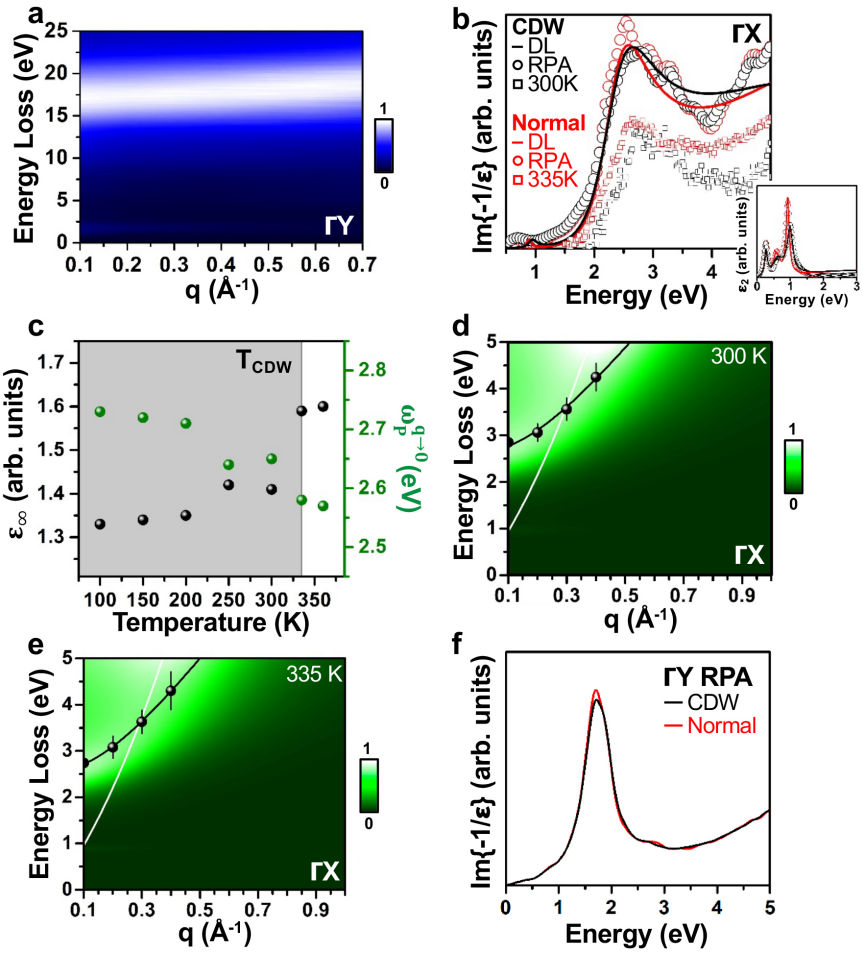

Supplementary Figure 6 | Experimental and theoretical studies of plasmon dispersions in CuTe. **a**, The dispersion map of the bulk plasmon along ΓY observed at 300 K. **b**, The RPA-theoretical loss functions of the Te-p_x light-electron plasmon along ΓX in respective CDW (black) and normal (red) states at q = 0.1 Å^{-1}. Open circles (squares), RPA calculations (EELS at designated temperatures, ZLP removed). Inset, the corresponding imaginary parts of the dielectric functions (ε_2; circles, RPA) predominated by three single-particle transitions below the plasmon excitation. Black and red lines, the Drude-Lorentz (DL) modeling of respective RPA dielectric functions (supplementary information C) and the readily derived loss functions. **c**, The temperature-dependent ε_∞ (black) and associated $\omega_p^{q\to 0}$ (green) used in the ε_∞ derivations (see also supplementary information C). **d** and **e**, The DL-simulated dispersion maps of the respective light-electron plasmons at 300 and 335 K using the v_F experimentally derived from Fig. 5a in the main text. Black dots, pseudo-Voigt-fitted plasmon peak positions. Black curves, the calculated plasmon dispersions using equation (1) in the main text. White curves, the respective single-particle continua. Error bars in **d** and **e**, standard errors in the plasmon-peak fitting. **f**, The RPA-calculated loss functions of the respective Te-p_y heavy-hole plasmons in the CDW (black) and normal (red) states along ΓY, showing a close similarity.

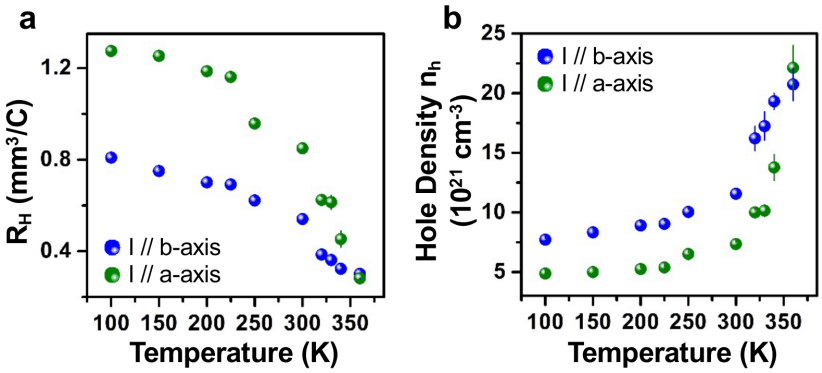

Supplementary Figure 7 | Hall measurements of CuTe. a, Hall coefficients measured with the currents flowing along a- and b-axes, respectively. The positive coefficients point out predominant hole contributions. **b**, The estimated hole densities along respective a- and b-axes.

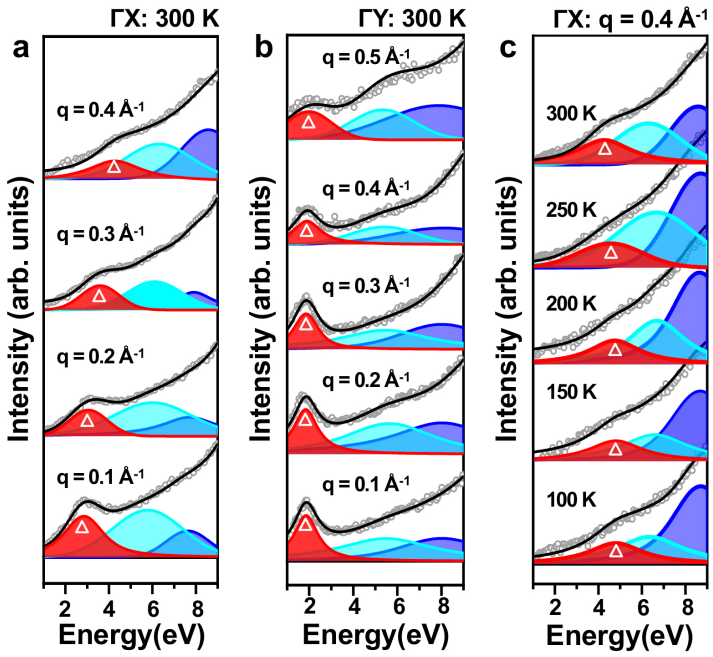

Supplementary Figure 8 | The pseudo-Voigt fitting of plasmon peaks in CuTe. a and **b**, The fitted Te-p_x light-electron and Te-p_y heavy-hole plasmons (red; white triangles, peak positions) at 300 K as a function of q, respectively. **c**, The fitted light-electron plasmons below T_{CDW} at q = 0.4 Å^{-1}. Open dots in **a**-**c**, experimental EELS spectra with the ZLP removal. Black curves in **a**-**c**, the fitted spectra. Cyan and blue peaks in **a**-**c**, high-energy interband transitions above the respective plasmons (red). No constraint on linewidths or positions of all the three spectral features (red, cyan, and blue) has been applied during the fitting.

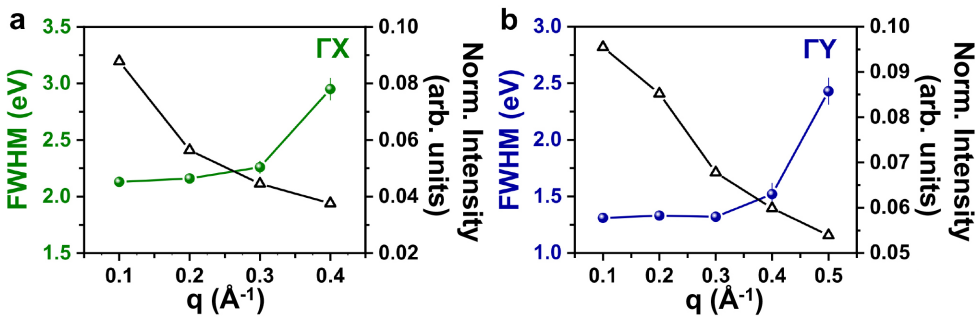

Supplementary Figure 9 | The full width at half maximum (FWHM) and fitted peak-intensity maxima of the plasmons at 300 K along respective ΓX and ΓY. a, The fitted FWHM linewidths (green) of the Te-p_x light-electron plasmons shown in Fig. 2e (300K; black dots, main text) as a function of q and derived from the plasmon-peak fittings in supplementary Fig. 8. The simultaneously derived plasmon-peak intensity maxima (black), normalized to those of the respective bulk plasmons acquired in the same time. **b**, The fitted FWHM linewidths (blue) and normalized peak-intensity maxima (black) of the Te-p_y heavy-hole plasmons shown in Fig. 2f (300 K; black dots, main text) as a function of q. Error bars, standard errors in the associated plasmon-peak fittings and those for the peak-intensity maxima omitted for simplicity. The observed plasmon broadening in **a** and **b** is consistent with the respective Landau damping depicted in Figs. 2e and 2f (main text). The concomitant plasmon weakening is also consistent with the classical physics for damped collective plasmon excitations[1].

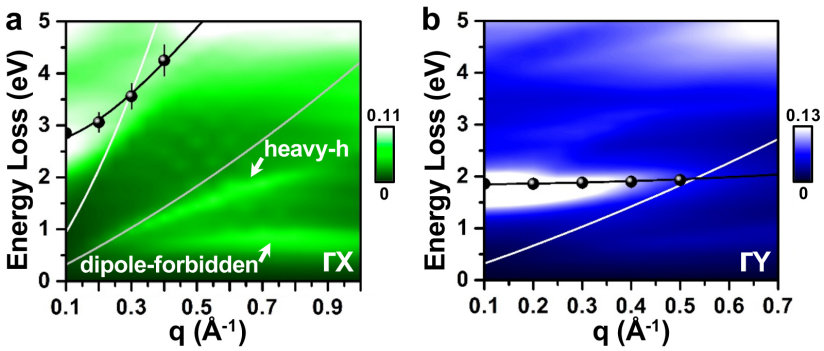

Supplementary Figure 10 | Theoretical plasmon-dispersion maps of the normal-state CuTe by RPA in the context of DFT. a and **b**, The RPA-calculated dispersion maps of the Te-p_x light-electron plasmon along ΓX and the Te-p_y heavy-hole plasmon along ΓY, respectively, in the normal state. Black dots, pseudo-Voigt-fitted plasmon peak positions of the CDW state at 300 K (error bars, standard errors in the peak fitting). Black curves, calculated dispersions using equation (1) on the basis of v_F in Table 1 in the main text. As shown in supplementary Figs. 6b and 6f, the difference in the plasmon excitations between the normal and CDW states is not overwhelming, though discernible, along ΓX and negligible along ΓY. These normal-state maps, which are computationally less expensive, are thus used for shedding more light on the CDW-state counterparts (Figs. 2e-f, main text). White curve in **a** (**b**), the single-particle continuum of the light electrons (heavy holes). Gray curve in **a**, the single-particle continuum of the heavy holes in **b**, highlighting the heavy-hole plasmon[5] in **a** being located to the right of the continuum. The heavy-hole plasmon is, therefore, to be subject to Landau damping and becomes experimentally unobservable in Fig. 2e (main text). The flat, dispersionless excitation slightly below 1 eV in **a** arises from the dipole-forbidden interband transition[5] and our apparatus is unable to tackle electronic excitations below 1 eV. The DL-simulated maps in supplementary Figs. 6d (CDW state) and 6e (normal state) otherwise capture the dispersion of the light-electron plasmon in **a**, indicating the quality of our DL modeling.

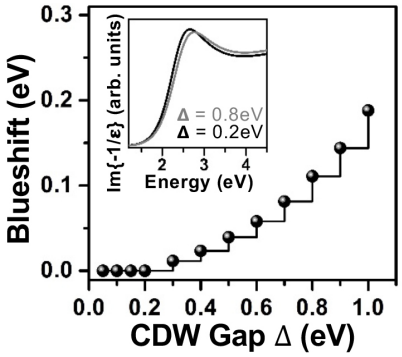

Supplementary Figure 11 | The DL modeling of plasmon blueshifts by the CDW gap opening. The calculated plasmon blueshift due to the presence of an additional single-particle oscillator strength by the CDW-gap opening below T_{CDW}. Blueshift, defined as the difference from the plasmon-peak position with Δ of 50 meV (i.e., 300 K's in Fig. 4c in the main text). Inset, the calculated EELS loss functions with Δ of 0.2 and 0.8 eV, respectively. In this DL modeling, a discernible plasmon blueshift above 0.1 eV has to involve a CDW gap above 0.7 eV, which is way beyond the experimental observation in Fig. 4c (main text). Accordingly, the characteristically small Δ of CuTe (Fig. 4c, main text) can hardly affect the Te-p_x light-electron plasmon that sits at a much higher energy than Δ.

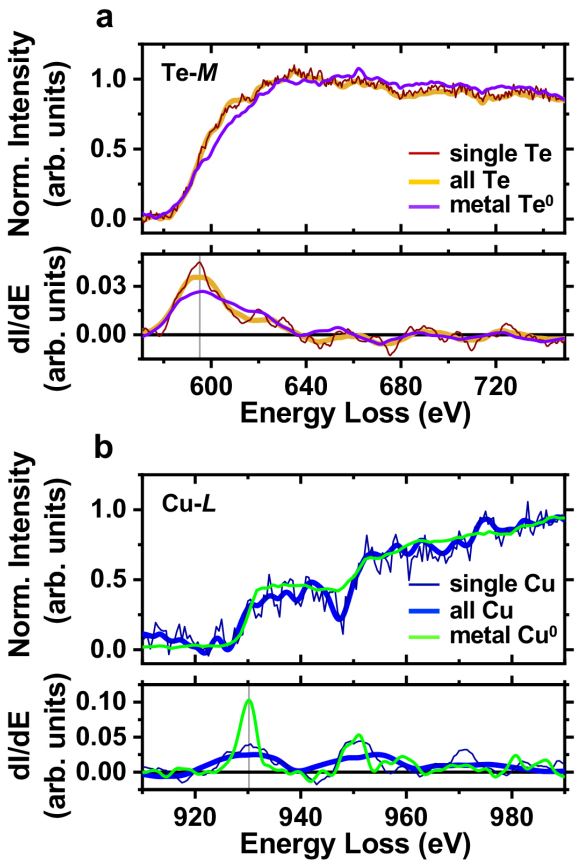

Supplementary Figure 12 | STEM-EELS spectra acquired in the CDW supercell at 300 K. a (top panel), The Te M-edge EELS spectra of upper-Te-1 atom (Fig. 5b, main text; thin dark red hereby) and all 20 Te atoms (thick yellow hereby) in the supercell. The reference-Te^0 spectrum acquired on a thin Te-metal foil (purple) is also shown. Bottom panel, the first derivative of the three Te M-edge spectra, with the onset energy of the metallic-Te^0 reference being denoted by a vertical line. **b** (top panel), The Cu L-edge EELS spectra of upper-Cu-1 atom (Fig. 5b, main text; thin dark blue hereby) and all 20 Cu atoms (thick blue hereby) in the supercell. The reference-Cu^0 spectrum taken on a thin Cu-metal foil (green) is exhibited. Bottom panel, the first derivative of the three Cu L-edge spectra, with the onset energy of the metallic-Cu^0 reference being denoted by a vertical line. The STEM-EELS datasets have been subject to the random-noise reduction by the principal-component analysis and then the power-law background removal prior to the respective Cu-L and Te-M edge retrievals[6-8]. The spectra of the Te-1 and Cu-1 atoms are the respective integrals of 2×2 pixels underneath (pixel size, ~0.4 Å) and those of all Te and Cu atoms are the integrals of all the associated atoms in the $5a \times 2c$ supercell of the CDW. The STEM-EELS mapping of Te and Cu (Fig. 5b, main text) is accomplished by integrating the respective spectral intensities centered at the indicated vertical lines in **a** and **b** (bottom panels) with the integral-window size of 2 eV.

A. The inelastic electron scattering upon the q-EELS experimental setup

As indicated in supplementary Fig. 1, a given electronic excitation (ΔE) is subject to the inelastic scattering with the momentum (q) and energy (ΔE) transfers to the material. The q is composed by the $q_{\parallel}$ and $q_{\perp}$, and the $q_{\parallel}$ is formulated by $\mathbf{q}_{\parallel} = \mathbf{k_0}\theta_{\Delta E}$, with the scattering angle $\theta_{\Delta E}$ being of $\theta_{\Delta E} = \frac{\Delta E}{2E_0}$ (E_0, the energy of the incident-electron beam; 200 kV hereby) and k_0 being the incident electron-beam wave vector[1]. The $\theta_{\Delta E}$ is characteristically very small and much smaller than the elastic Bragg-scattering angle of $2\theta_B$ ($2d \sin\theta_B = \lambda$, where d being the atomic-plane spacing and λ the electron wavelength of 0.0251 Å at 200 kV), rendering the $q_{\parallel}$ to be practically parallel to k_0. The q for q-EELS is, therefore, largely dominated by the $q_{\perp}$ with $\mathbf{q}_{\perp} = \mathbf{k_0}\theta$ and $\mathbf{q} = \sqrt{\mathbf{q}_{\perp}^2 + \mathbf{q}_{\parallel}^2}$.

The experimental undertaking of q-EELS is achieved by collecting the inelastically scattered electrons at the designated $q_{\perp}$ in between two Bragg spots that depict the symmetry line of interest in reciprocal space (Fig. 2a, main text). For warranting an ultimate correctness in the q-EELS probing, $q_{\perp}$ is to be larger than the momentum resolution (Δq) of the experimental setup and, ubiquitously, $\Delta q \gg q_{\parallel}$. In our experiments, Δq is of ~0.09 Å^{-1} upon the exploitation of a circular EELS-collection aperture of 2.5 mm in diameter and a diffraction-pattern projection length of 6.8 m ($\Delta q \approx \frac{0.0025}{6.8} \times k_0 \approx 0.09$ Å^{-1}). For tackling the light-electron and also heavy-hole plasmons, the $q_{\perp}$ is readily optimized as 0.1 Å^{-1} and leads to the condition of $\mathbf{q} = \sqrt{\mathbf{q}_{\perp}^2 + \mathbf{q}_{\parallel}^2} \approx \mathbf{q}_{\perp}$ with $q_{\perp} \gg q_{\parallel}$. In Figs. 2c-2g and 3 in the main text and supplementary Fig. 6a, the spectral acquisitions were achieved by displacing the diffraction pattern along ΓX or ΓY with the $q_{\perp}$ step of 0.1 Å^{-1} (i.e., $q \approx q_{\perp} \gg q_{\parallel}$) and, for simplicity, we denote q instead of $q_{\perp}$ throughout the work, as the q-EELS convention[1].

B. Theoretical calculations of the complex dielectric functions and EELS loss functions

This paragraph outlines the theoretical principles for supplementary Figs. 3, 5, 6b, 6f, and 10. The complex dielectric function is written in $\varepsilon(\omega, \mathbf{q}) = \varepsilon_1(\omega, \mathbf{q}) + i\varepsilon_2(\omega, \mathbf{q})$. Without including the electron-hole interaction, $\varepsilon(\omega, \mathbf{q})$ can be calculated in the RPA as shown below.

$$\varepsilon_{\mathbf{GG'}}(\omega, \mathbf{q}) = \delta_{\mathbf{GG'}} - v(\mathbf{q}+\mathbf{G}) \sum_{m}^{occ} \sum_{m'}^{emp} \sum_{\mathbf{k}}^{BZ} M_{mm'}(\mathbf{k}, \mathbf{q}, \mathbf{G}) M^*_{mm'}(\mathbf{k}, \mathbf{q}, \mathbf{G'}) \times \frac{1}{2}\left[\frac{1}{E_{m\mathbf{k}+\mathbf{q}} - E_{m'\mathbf{k}} - \omega \mp i\delta} + \frac{1}{E_{m\mathbf{k}+\mathbf{q}} - E_{m'\mathbf{k}} + \omega \pm i\delta}\right]$$

, where $\mathbf{G}(\mathbf{G'})$ and $v(\mathbf{q}+\mathbf{G})$ are the lattice vectors and Coulomb potential. $M_{m,m'}(\mathbf{k}, \mathbf{q}, \mathbf{G})$ is the

polarizability matrix element between occupied (m) and unoccupied (m′) states. E_{mk} are the electronic eigenvalues. The macroscopic component of the complex dielectric function at $\mathbf{G} = \mathbf{G}' = 0$ can be computed by a full-frequency calculation in the Berkeley GW package[9]. In supplementary Fig. 3, the further inspections on intraband- or interband-transition characteristics of the dielectric functions are conducted by band decompositions on the basis of the polarizability matrix[10]. The following-on calculation of the EELS loss function is straightforward by the following formulation.

$$-\operatorname{Im}\frac{1}{\varepsilon(\omega,\mathbf{q})}=\frac{\varepsilon_2(\omega,\mathbf{q})}{\varepsilon_1^2(\omega,\mathbf{q})+\varepsilon_2^2(\omega,\mathbf{q})}$$

The acoustic-like heavy-hole plasmon. The calculated plasmon-dispersion maps in supplementary Fig. 10a deserve further explanations. Along ΓX, Te-p_x light electrons and Te-p_y heavy holes indeed coexist (Figs. 1c-d, main text). In addition to the light-electron plasmon along ΓX, the coexisting heavy holes would give rise to an acoustic-like heavy-hole plasmon with a practically linear dispersion from ~0.1 to ~0.8 Å^{-1} (supplementary Fig. 10a)[5], which has been theoretically proposed by David Pine in 1956 to arise from the screening between coexisting light- and heavy-carrier plasmons in the same matter[11]. Our calculations in supplementary Fig. 10a indicate that this acoustic-like plasmon locates in the Landau-damping regime (i.e., to the right of the corresponding single-particle continuum) and is to be heavily damped, thus experimentally unobservable in Fig. 2e (main text).

C. Drude-Lorentz modeling of the complex dielectric functions along ΓX

This section elaborates on the Drude-Lorentz (DL) modeling of $\varepsilon(\omega)$ in both the normal and CDW states along ΓX in supplementary Fig. 6b. The following equation[12] is exploited in the simulation.

$$\varepsilon(\omega)=1-\frac{\omega_P^2}{\omega^2+i\gamma_P\omega}-\frac{\omega_\Delta^2}{\omega^2-\omega_\Delta^2+i\gamma_\Delta\omega}-\sum_{l=1}^{4}\frac{\omega_{T,l}^2}{\omega^2-\omega_{T,l}^2+i\gamma_{T,l}\omega}$$

The second term of the equation denotes the free-electron-gas (FEG) Drude component, with ω_P and γ_P being the respective plasmon frequency and damping constant. The third term represents the single-particle Lorentz contribution ascribed to the excitation across the CDW gap (Δ), with ω_Δ corresponding to the gap size and γ_Δ depicting the associated damping[12]. The forth term is attributed to the three distinct absorptive peaks below 2 eV in RPA (inset, supplementary Fig. 6b) and also the single-particle excitation right above the plasmon (supplementary Fig. 8a), with ω_T and γ_T being the respective oscillator strength and damping constant. All the physical parameters used in the DL modeling are shown in supplementary Table 1 below.

Supplementary Table 1 | The physical parameters for the DL modeling of $\varepsilon(\omega)$ in the respective normal and CDW states (all units in eV).

Phase	ω_P	γ_P	ω_Δ	γ_Δ	ω_{T1}	γ_{T1}	ω_{T2}	γ_{T2}	ω_{T3}	γ_{T3}	ω_{T4}	γ_{T4}
Normal	3.25	0.01	0	0.2	0.27	0.2	0.59	0.25	0.92	0.11	4.5	5.5
CDW	3.15	0.01	0.05	0.2	0.27	0.1	0.66	0.4	0.99	0.2	4.5	6.3

Estimation of the temperature-dependent ε_∞. The achievements in the DL modeling of the RPA dielectric functions in supplementary Fig. 6b (inset, open circles) have exploited the respective Drude ω_P components of 3.25 and 3.15 eV in the normal and CDW states (supplementary Table 1). The readily DL-derived loss functions (solid lines, supplementary Fig. 6b) capture the respective RPA counterparts (open circles) and are consistent with the experimental ZLP-removed EELS spectra (open squares; normal, 335 K; CDW, 300 K). The respective Drude-ω_P components in supplementary Table 1 are then exploited for the normal (335 and 360 K) and CDW states (100-300 K) in general, since it is implausible to obtain the RPA dielectric function at each designated temperature.

Subsequently, we elaborate on the linear extrapolation of the light-electron plasmon at q = 0 Å^{-1}, i.e., $\omega_P^{q\to0}$ in the ω^2–q^2 scaling of EELS, and find 2.58 (2.65) eV at 335 (300) K, for instance, as shown in supplementary Fig. 6c (green). All the linearly-extrapolated $\omega_P^{q\to0}$ values are smaller than the respective Drude-ω_P components in the normal and CDW states due to the screening effect imposed by single-particle transitions above the plasmons (for brevity, ω_{T4} in our DL modeling). The associated screening dielectric constant (ε_∞) for the corresponding light-electron plasmon can then be derived using the equation below[1], leading to $\varepsilon_\infty \sim 1.59$ for the normal state at 335 K and 1.41 for the CDW state at 300 K. The complete temperature-dependent ε_∞ is further exhibited in supplementary Fig. 6c (black).

$$\omega_P^{q\to0} = \frac{\omega_P}{\sqrt{\varepsilon_\infty}}$$

Blueshifts of the light-electron plasmon. In supplementary Fig. 11, the blueshifts of the Te-p_x light-electron plasmon with decreasing temperatures have been derived from the loss functions using the DL modeling of $\varepsilon(\omega)$ with increasing ω_Δ and, meanwhile, γ_Δ being kept constant for simplicity. It may be argued that the CDW-gap opening (Fig. 4c, main text) can add on a single-particle transition to $\varepsilon(\omega)$ and pushes the light-electron plasmon to a higher energy[1,12,13], resulting in the blueshifts with decreasing temperatures in Fig. 4d (main text). In supplementary Fig. 11, the calculated plasmon blueshifts with the gap Δ as a tunable additional oscillator strength in $\varepsilon(\omega)$ indicate that a gap size Δ above 0.7 eV is required for inducing a blueshift above 0.1 eV in Fig. 4d (main text), while the Δ is no more than 0.2 eV (Fig. 4c, main text). Unambiguously, the plasmon blueshifts below 300 K in Fig. 4d (main text) are not an effect of the Δ. This analytical approach is effective considering DFT is inconvenient in adapting a tunability in Δ.

DL simulations of the plasmon-dispersion maps. In supplementary Figs. 6d and 6e, the dispersion maps of the Te-p_x light-electron plasmon were calculated using the DL formulation in this section C with the q dependence in the $\varepsilon(\omega)$ being approximated by a q dependence in the Drude term in accordance with equation (1) in the main text. The temperature-dependent v_F required for this DL simulation was derived from Fig. 5a in the main text and the CDW-gapping term (Δ) in the $\varepsilon(\omega)$ was obtained from Fig. 4c (main text). For simplicity, the fourth term in the $\varepsilon(\omega)$ equation has been assumed to be q-independent. The thus-calculated maps show a notable consistency with the superimposed experimental dispersions (black dots and lines), with the incorporation of respective single-particle continua (white lines).

D. The effective bulk electronic density of CuTe

The effective bulk electronic density (r_s), $r_s = \frac{m^* e^2}{\hbar^2 \varepsilon_0}\left(\frac{3}{4\pi n}\right)^{1/3}$ where ε_0 is the static dielectric constant, of FEG-like metals showing the characteristic plasmon dispersion of equation (1) in the main text typically falls in the range of $2 \leq r_s \leq 6$ (customarily, $m^* = m_0$ and $\varepsilon_0 = 1$)[13]. Semimetals that display the RPA dispersion are otherwise of $r_s \ll 1$ due to the characteristic m^* and ε_0 (e.g., semimetal Bi, $r_s \sim 0.1$ with $m^* \sim 0.1\ m_0$ and $\varepsilon_0 \sim 100$)[13]. In semimetal CuTe, the $\omega^2 - q^2$ scaling of the bulk-plasmon dispersions (Fig. 2h, main text) reveals isotropic dispersions along ΓX and ΓY and yields $m^* = 1.12\ m_0$ and $n = 2.37 \times 10^{23}$ cm^{-3} in average for the corresponding valence electrons (exploiting $\varepsilon_\infty = 1$ considering the absence of screening interband transitions; insets, supplementary Figs. 5a and 5b). With these m^*, n, and ε_0 of ~150 (supplementary Fig. 5a), the bulk CuTe features $r_s \sim 0.014 \ll 1$, which is consistent with the established wisdom on semimetals[13] and underlines the satisfactory FEG-based dispersions of the bulk, light-electron, and heavy-hole plasmons in Figs. 2h and 4a in the main text. The FEG-like essence of CuTe is in line with the negligible effects of exchange-correlations and Coulomb interactions in the band-structure calculations (Figs. 1c-e and 1g, main text) and the weak charge localization of the CDW (Figs. 5b and 5c, main text; supplementary Fig. 12).

E. The CDW electrostatic potential

The electrostatic potential built across parallel charged sheets is evaluated by $V = \frac{n_{2D} e d}{\varepsilon_0 \varepsilon}$, where n_{2D} is the planar carrier concentration and d is the distance between the sheets[6]. This classical formulation is borrowed for the estimation of the CDW potential. With the approximate charge variation of ±0.03 at maximum in the CDW (Figs. 5b and 5c, main text; also supplementary Fig. 12), the n_{2D} could correspond to $\frac{0.03}{bc}$ (b, c, and later a, lattice parameters of CuTe). Supposing the sheets locate at the peak and valley of an individual sinusoidal CDW wave in Fig. 1b (main text), the d would then be of 2.5a and, together with the n_{2D}, we derive the V of ~0.01 eV. Due to the presence

of two anti-phase coupled sinusoidal waves in the CDW supercell (Fig. 1b, main text), the characteristic electrostatic potential would amount to 2V ~ 0.02 eV at maximum. This potential barrier height of ~0.02 eV is slightly inferior to the thermal energy at room temperature (300 K ~ 0.026 eV), providing the CDW fluctuation near T_{CDW} and the frozen-in CDW below 200 K ~ 0.017 eV (Fig. 5d) with an electrostatic clue.

Supplementary References

1. Raether, H. *Excitation of Plasmons and Interband Transitions by Electrons* (Springer-Verlag, Berlin Heidelberg New York, 1980).
2. Reimer, L. *Transmission Electron Microscopy* (Chapter 7, Theory of Electron Diffraction; 4th edition, Springer, Berlin, 1997).
3. Gloter, A., Douiri, A., Tencé, M. & Colliex, C. Improving energy resolution of EELS spectra: an alternative to the monochromator solution. *Ultramicroscopy* **96**, 385-400 (2003).
4. Ishizuka, K., Kimoto, K. & Bando, Y. Improving energy resolution of EELS spectra by deconvolution using maximum-entropy and Richardson-Lucy algorithms. *Microsc. Microanal*. **9** (Suppl. 2), 832-833 (2003).
5. Cudazzo, P. & Wirtz, L. Collective electronic excitations in charge density wave systems: The case of CuTe. *Phys. Rev. B* **104**, 125101 (2021).
6. Lee, P.-W. *et al*. Hidden lattice instabilities as origin of the conductive interface between insulating $LaAlO_3$ and $SrTiO_3$. *Nat. Commun.* **7**, 12773 (2016).
7. Chu, M.-W. *et al*. Probing charge order and hidden topology at the atomic scale by cryogenic scanning transmission electron microscopy and spectroscopy. *Phys. Rev. B* **103**, 115130 (2021).
8. Chang, C.-P. *et al*. Atomic-scale observation of a graded polar discontinuity and a localized two-dimensional electron density at an insulating oxide interface. *Phys. Rev. B* **87**, 075129 (2013).
9. Deslippe, J. *et al*. BerkeleyGW: A massively parallel computer package for the calculation of the quasiparticle and optical properties of materials and nanostructures. *Comput. Phys. Commun.* **183**, 1269-1289 (2012).
10. da Jornada, F. H., Xian, L, Rubio, A. & Louie, S. G. Universal slow plasmons and giant field enhancement in atomically thin quasi-two-dimensional metals. *Nat. Commun.* **11**, 1013 (2020).
11. Husain, A. A. *et al*. Pine's demon observed as a 3D acoustic plasmon in Sr_2RuO_4. *Nature* **621**, 66-70 (2023).
12. Lin, Z. *et al*. Dramatic plasmon response to the charge-density-wave gap development in 1T-$TiSe_2$. *Phys. Rev. Lett.* **129**, 187601 (2022).
13. Platzman, P. M. & Wolff, P. A. *Waves and Interactions in Solid State Plasma* (Academic Press, New York and London, 1973).